DEPARTMENT OF INFORMATICS

TECHNISCHE UNIVERSITÄT MÜNCHEN

Bachelor's Thesis in Informatics

Wave Reversal in Anisotropic Elastic Material using the Instantaneous Time Mirror

Milena Rode-Kotzé

DEPARTMENT OF INFORMATICS

TECHNISCHE UNIVERSITÄT MÜNCHEN

Bachelor's Thesis in Informatics

Wave Reversal in Anisotropic Elastic Material using the Instantaneous Time Mirror

Zeitumkehr von Wellen in anisotropem elastischem Material mithilfe des Instantanen Zeitspiegels

Author:	Milena Rode-Kotzé
Supervisor:	Prof. Dr. Michael Bader
Advisor:	Vikas Kurapati, M.Sc.
Submission Date:	30.09.2024

I confirm that this bachelor's thesis in informatics is my own work and I have documented all sources and material used.

Garching , 30.09.2024 Milena Rode-Kotzé

Acknowledgments

First and foremost, I would like to thank Vikas Kurapati, my thesis supervisor, for his invaluable guidance, constructive feedback, and continuous encouragement throughout the entirety of this thesis. His expertise and advice have been instrumental in shaping both the direction and content of this thesis.

I owe a special debt of gratitude to my family and friends for their endless patience, unwavering support and encouragement throughout my studies. Their continuous curiosity, even when details were difficult to follow, kept me motivated.

Abstract

In the pursuit of increasingly accurate seismic event modeling, incorporating anisotropy is critical for accurately describing the Earth's subsurface structure. This thesis explores the Instantaneous Time Mirror (ITM) method for numerical wave reversal in anisotropic media, implemented within the open-source simulation software SeisSol. The study analyzes seismic waves in both forward and backward directions, achieving wave refocusing under varying velocity conditions to recreate the initial source event. The ITM approach is validated against benchmarks and applied in a real-world context around Mount Zugspitze.

Contents

1 Introduction

The continuous study and analysis of seismic events aims to identify and reduce potential damages and casualties. Accurate seismic event modeling is critical for understanding the phenomena and enhancing mitigation strategies.

SeisSol is a powerful simulation tool that models seismic phenomena, generating seismological data using tetrahedral meshes to resemble realistic 3D model events and supports all major rheologies, including isotropic and anisotropic elastic, poroelastic and viscoplastic properties. To work around this computationally intensive task, SeisSol uses the ADER-DG approach, combining the Discontinuous Galerkin (DG) method with the Arbitrary high-order schemes using DERivatives (ADER) time-integration approach. This method uses a piecewise polynomial approximation at each element achieving arbitrary high-order accuracy in both time and space.

Seismic time-reversal can be used to find the source of the waves and has two basic approaches, the time-reversal mirror and the Instantaneous Time Mirror (ITM). The time-reversal mirror involves recording and then reversing the velocity of each particle, thus reversing the entire wave field. The ITM on the other hand mimics the role of Loschmidt's demons by abruptly modifying wave properties, thus creating a time-reversed wave that refocuses at the origin and then diverges again. The ITM has been shown to be effective on water surface waves and does not require antennas or receivers.

SeisSol has already been extended to support wave reversal using the ITM method for isotropic elastic waves. A reflection of either both, only the P- or only the S-wave is achieved by modifying the material properties for a small time step, thus changing the wave impedance.

For more accurate seismic simulations, it is essential to consider anisotropy in modeling the Earth's subsurface. Anisotropy arises due to layers, cracks, internal crystal structures, and ice crystal alignment, and it plays a significant role in affecting wave speed and scattering.

As SeisSol has recently been extended to also simulate anisotropy [WGB20], the goal of this thesis is to extend the ITM feature in SeisSol to account for anisotropic elastic materials. To achieve ITM in a simulation environment, the seismic wave impedances are modified for a short period from t_{ITM} to $t_{\text{ITM}} + \tau$ by altering the material properties that govern anisotropic behavior. In anisotropic media, these properties are no longer limited to just λ, μ, and ρ as in isotropic materials, but instead involve more complex stiffness tensor components that dictate how waves propagate differently in various directions.

The thesis is structured as follows: Chapter 2 lays the foundation of elastic wave propagation and the ADER-DG method. Chapter 3 discusses the ITM method from a theoretical

perspective. The implementation in SeisSol is laid out in Chapter 4. Chapter 5 presents the results of different modeling scenarios. Chapter 6 concludes the thesis and suggests potential areas for future research.

2 Seismic Waves and ADER-DG formulation

In this chapter, the required theoretical foundations for the thesis are derived. The basic equations of elastic wave propagation are laid out and the basic equations of motion are formulated in the velocity-stress formulation.

Consequently, the fundamental framework of the simulation software used for the implementation is established. SeisSol simulates seismic wave phenomena using the ADER-DG method, which combines the Arbitrary high-order DERivatives (ADER) approach with the Discontinuous Galerkin (DG) method. This approach integrates the DG finite element method with a time-integration scheme based on the solution of arbitrary high-order derivatives of Riemann problems, ensuring high accuracy in both time and space [DK06a], [Käs+10].

2.1 Elastic Wave Equation

The key characteristic of an elastic material is a natural state where strains and stresses are zero, which it returns to when all applied forces are removed. For infinitesimal strains and stresses, the theory of linear elasticity can be applied. The displacement vector **U** is defined to describe the shortest distance between initial and current position of a point. The particle velocities u, v and w in directions x, y and z can then be defined as the temporal derivative of **U**

$$\begin{aligned} \frac{\partial U_x}{\partial t} &= \dot{U}_x = u, \\ \frac{\partial U_y}{\partial t} &= \dot{U}_y = v, \\ \frac{\partial U_z}{\partial t} &= \dot{U}_z = w. \end{aligned} \tag{2.1}$$

Here the subscript stands for the coordinate direction and the dot represents it's partial time derivative. Thus, the velocity vector $\mathbf{V} = [V_1, V_2, V_3] = [u, v, w]$ can be introduced for simplification.

A body is linearly elastic, if each stress tensor component σ_{ij} is a linear combination of all strain tensor components ϵ_{ij}, i.e. if the following extension of Hooke's law holds

$$\sigma_{ij} = c_{ijkl}\epsilon_{kl} \tag{2.2}$$

where c_{ijkl} are the medium specific constants of a fourth-order and have the symmetries

$$\begin{aligned} c_{jikl} &= c_{ijkl}, \\ c_{ijlk} &= c_{ijkl}, \\ c_{ijkl} &= c_{klij}. \end{aligned} \tag{2.3}$$

This reduces the number of independent components in c_{ijkl} from 81 to 21. As the constants c_{ijkl} remain constant over time, the time derivative of the stress tensor trivially becomes

$$\partial_t \sigma_{ij} = c_{ijkl} \partial_t \epsilon_{kl} \tag{2.4}$$

Note that the Einstein summation convention is followed here, i.e. an index appearing twice is summed over all possible values.

Continuing with infinitesimally small perturbations, the strain tensor is defined to have the components

$$\epsilon_{kl} = \frac{1}{2}(\partial_k U_l + \partial_l U_k), \tag{2.5}$$

where ∂_k denotes the spatial derivative in k-direction and U_i represents the displacement in i-direction. To return to the consistently used velocity-stress formulation, we move away from the displacement-stress formulation and thus substitute the displacements U_i with the previously introduced velocities V_i, which yields the time derivative of the strain tensor, which is dependant on the spatial derivative of said velocities V_i

$$\partial_t \epsilon_{kl} = \frac{1}{2}(\partial_k V_l + \partial_l V_k). \tag{2.6}$$

The resulting relation can be written in a matrix-vector matter using the Voigt notation:

$$\begin{pmatrix} \sigma_{11} \\ \sigma_{22} \\ \sigma_{33} \\ \sigma_{23} \\ \sigma_{13} \\ \sigma_{12} \end{pmatrix} = \begin{pmatrix} c_{11} & c_{12} & c_{13} & c_{14} & c_{15} & c_{16} \\ & c_{22} & c_{23} & c_{24} & c_{25} & c_{26} \\ & & c_{33} & c_{34} & c_{35} & c_{36} \\ sym & & & c_{44} & c_{45} & c_{46} \\ & & & & c_{55} & c_{56} \\ & & & & & c_{66} \end{pmatrix} \begin{pmatrix} \varepsilon_{11} \\ \varepsilon_{22} \\ \varepsilon_{33} \\ 2\varepsilon_{23} \\ 2\varepsilon_{13} \\ 2\varepsilon_{12} \end{pmatrix}. \tag{2.7}$$

Next the equation of motion for a volume V bound by a surface S shall be obtained. The rate of change of momentum of particles in V equals the forces acting upon said particles. Said forces are composed of a body as well as a surface force, resulting from the presence of normal and sheer stresses. This is expressed in

$$\frac{\partial}{\partial t} \int_V \rho \frac{\partial \mathbf{U}}{\partial t} dV = \int_V \mathbf{f} dV + \oint_S \mathbf{T}(\mathbf{n}) dS. \tag{2.8}$$

Here $\frac{\partial}{\partial t} \int_V \rho \frac{\partial \mathbf{U}}{\partial t} dV$ denotes the momentum of the control volume with density ρ. $\mathbf{T}$ is the traction vector which is related to the stress tensor by Cauchy's stress theorem

$$T_i = \sigma_{ij} n_i \tag{2.9}$$

with normal vector n_i.

We now replace $\mathbf{T}$ in 2.8, thus obtaining

$$\oint_S \mathbf{T}(\mathbf{n}) dS = \oint_S \sigma_{ij} n_i dS. \tag{2.10}$$

and apply Gauss's divergence theorem so that this becomes

$$\oint_S \sigma_{ij} n_i dS = \int_V \partial_j \sigma_{ij} dV. \tag{2.11}$$

By inserting this resulting equality into 2.8, utilizing the symmetry of the stress tensor $\sigma_{ij} = \sigma_{ji}$ and rearranging the terms, the following equation is obtained

$$\int_V \left(\rho \frac{\partial^2 U_i}{\partial t^2} - f_i - \partial_j \sigma_{ij} \right) dV = 0. \tag{2.12}$$

This integrand must be zero at every point where it is continuous, thus

$$\rho \frac{\partial^2 U_i}{\partial t^2} = f_i + \partial_j \sigma_{ij}, \tag{2.13}$$

where we can expand the equation in j and replace $\frac{\partial U_i}{\partial t}$ by V_i to obtain

$$\rho \frac{\partial V_i}{\partial t} = f_i + \partial_x \sigma_{xi} + \partial_y \sigma_{yi} + \partial_z \sigma_{zi}. \tag{2.14}$$

To analyze the eigenstructure of the system this needs to be conformed to a more compact form of hyperbolic equations. Combining 2.7 with the equation of motion [Pue+07] results in a complete partial differential equation system

$$\frac{\partial Q_p}{\partial t} + A_{pq} \frac{\partial Q_q}{\partial x} + B_{pq} \frac{\partial Q_q}{\partial y} + C_{pq} \frac{\partial Q_q}{\partial z} = 0 \tag{2.15}$$

where Q defines the p quantities of interest, that is the vector of unknown stresses and velocities $Q = (\sigma_{xx}, \sigma_{yy}, \sigma_{zz}, \sigma_{xy}, \sigma_{yz}, \sigma_{xz}, u, v, w)^T$ and A_{pq}, B_{pq} and C_{pq} are space-dependent Jacobian matrices given by

$$A_{pq} = \begin{bmatrix} 0 & 0 & 0 & 0 & 0 & 0 & -c_{11} & -c_{16} & -c_{15} \\ 0 & 0 & 0 & 0 & 0 & 0 & -c_{12} & -c_{26} & -c_{25} \\ 0 & 0 & 0 & 0 & 0 & 0 & -c_{13} & -c_{36} & -c_{35} \\ 0 & 0 & 0 & 0 & 0 & 0 & -c_{16} & -c_{66} & -c_{56} \\ 0 & 0 & 0 & 0 & 0 & 0 & -c_{14} & -c_{46} & -c_{45} \\ 0 & 0 & 0 & 0 & 0 & 0 & -c_{15} & -c_{56} & -c_{55} \\ -\frac{1}{\rho} & 0 & 0 & 0 & 0 & 0 & 0 & 0 & 0 \\ 0 & 0 & 0 & -\frac{1}{\rho} & 0 & 0 & 0 & 0 & 0 \\ 0 & 0 & 0 & 0 & 0 & -\frac{1}{\rho} & 0 & 0 & 0 \end{bmatrix}, \tag{2.16}$$

$$B_{pq} = \begin{bmatrix} 0 & 0 & 0 & 0 & 0 & 0 & -c_{16} & -c_{12} & -c_{14} \\ 0 & 0 & 0 & 0 & 0 & 0 & -c_{26} & -c_{22} & -c_{24} \\ 0 & 0 & 0 & 0 & 0 & 0 & -c_{36} & -c_{32} & -c_{34} \\ 0 & 0 & 0 & 0 & 0 & 0 & -c_{66} & -c_{26} & -c_{46} \\ 0 & 0 & 0 & 0 & 0 & 0 & -c_{46} & -c_{24} & -c_{44} \\ 0 & 0 & 0 & 0 & 0 & 0 & -c_{56} & -c_{25} & -c_{45} \\ 0 & 0 & 0 & -\frac{1}{\rho} & 0 & 0 & 0 & 0 & 0 \\ 0 & -\frac{1}{\rho} & 0 & 0 & 0 & 0 & 0 & 0 & 0 \\ 0 & 0 & 0 & 0 & -\frac{1}{\rho} & 0 & 0 & 0 & 0 \end{bmatrix}, \tag{2.17}$$

$$C_{pq} = \begin{bmatrix} 0 & 0 & 0 & 0 & 0 & 0 & -c_{15} & -c_{14} & -c_{13} \\ 0 & 0 & 0 & 0 & 0 & 0 & -c_{25} & -c_{24} & -c_{23} \\ 0 & 0 & 0 & 0 & 0 & 0 & -c_{35} & -c_{34} & -c_{33} \\ 0 & 0 & 0 & 0 & 0 & 0 & -c_{56} & -c_{46} & -c_{36} \\ 0 & 0 & 0 & 0 & 0 & 0 & -c_{45} & -c_{44} & -c_{34} \\ 0 & 0 & 0 & 0 & 0 & 0 & -c_{55} & -c_{45} & -c_{35} \\ 0 & 0 & 0 & 0 & 0 & -\frac{1}{\rho} & 0 & 0 & 0 \\ 0 & 0 & 0 & 0 & -\frac{1}{\rho} & 0 & 0 & 0 & 0 \\ 0 & 0 & -\frac{1}{\rho} & 0 & 0 & 0 & 0 & 0 & 0 \end{bmatrix}. \tag{2.18}$$

The propagation velocities of elatstic waves are determined by the eigenvalues of said flux matrices. It should be noted that analytically ydetermining the eigenstructure of these Jacobian matices is more complex than in the isotropic case [Pue+07].

2.2 ADER-DG

This section provides an overview over the ADER-DG method used in SeisSol.

2.2.1 Discontinuous Galerkin Method

Unlike traditional finite-element methods, the Discontinuous Galerkin (DG) method solves hyperbolic systems while allowing piecewise polynomials within each element, which enhances flexibility in handling complex geometries and provides high-order accuracy. By coupling this method with generalized Riemann solvers (as in the ADER approach [TMN01]), the ADER-DG method advances the solution using an explicit, one-step scheme. This process requires interelement flux computations, ensuring accuracy in both time and space without needing multiple time steps.

We divide the computational domain $\Sigma \in \mathbb{R}^3$ into conforming tetrahedral elements $\mathcal{T}^{(m)}$ with unique indices $m \in \mathbb{N}$ and assume A, B, C to be piecewise constant in said $\mathcal{T}^{(m)}$. The tetrahedrons are transformed from a global, Cartesian system into reference elements $\mathcal{T}_E$ using a new coordinate system of (ξ, η, ζ). This process is visualized in 2.1.

As a result we require a new matrix $\tilde{A}^{(m)}$ with identical structure as 2.16 but with rotated

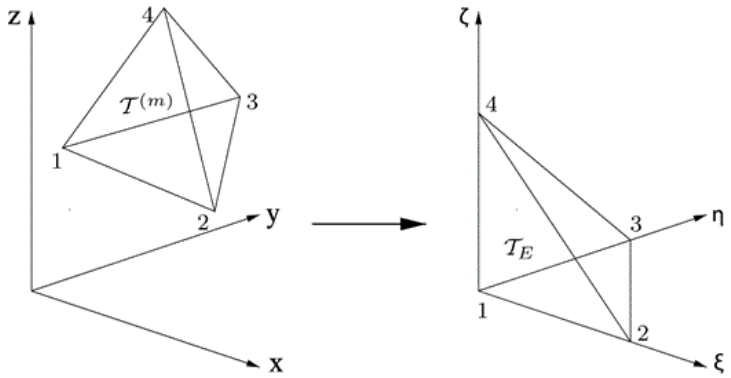

Figure 2.1: Transformation of tetrahedron into reference frame. (Figure taken from Figure 1 in [DK06a])

entries c_{ij}, thus transforming it from the global reference coordinate system to the local transformed coordinate system of the jth face of tetrahedron (m). To define said local coordinate system we use a normal vector $n = (n_x, n_y, n_z)^T$ and two tangential vectors $s = (s_x, s_y, s_z)^T$ and $t = (t_x, t_y, t_z)^T$. They lie in the plane determined by the face of the tetrahedron and are all orthogonal to each other. This rotation is obtained by applying the Bond's matrix ([Bon76], [OM03])

$$\mathcal{N} = \begin{pmatrix} n_x^2 & n_y^2 & n_z^2 & 2n_z n_y & 2n_z n_x & 2n_y n_x \\ s_x^2 & s_y^2 & s_z^2 & 2s_z s_y & 2s_z s_x & 2s_y s_x \\ t_x^2 & t_y^2 & t_z^2 & 2t_z t_y & 2t_z t_x & 2t_y t_x \\ s_x t_x & s_y t_y & s_z t_z & s_y t_z + s_z t_y & s_x t_z + s_z t_x & s_y t_x + s_x t_y \\ t_x n_x & t_y n_y & t_z n_z & n_y t_z + n_z t_y & n_x t_z + n_z t_x & n_y t_x + n_x t_y \\ n_x s_x & n_y s_y & n_z s_z & n_y s_z + n_z s_y & n_x s_z + n_z s_x & n_y s_x + n_x s_y \end{pmatrix} \tag{2.19}$$

to the Hook's matrix C of the global reference system

$$\mathcal{C} = \begin{pmatrix} c_{11} & c_{12} & c_{13} & c_{14} & c_{15} & c_{16} \\ c_{12} & c_{22} & c_{23} & c_{24} & c_{25} & c_{26} \\ c_{13} & c_{23} & c_{33} & c_{34} & c_{35} & c_{36} \\ c_{14} & c_{24} & c_{34} & c_{44} & c_{45} & c_{46} \\ c_{15} & c_{25} & c_{35} & c_{45} & c_{55} & c_{56} \\ c_{16} & c_{26} & c_{36} & c_{46} & c_{56} & c_{66} \end{pmatrix}, \tag{2.20}$$

which leads to

$$\tilde{C} = \mathcal{N} \cdot C \cdot \mathcal{N}^T, \tag{2.21}$$

the rotated Hooke's matrix which lies in the local reference system of the tetrahedron's boundary face.

The numerical solution Q_h of 2.15 is approximated in each $T_{(m)}$ using a linear combination of space-dependent but time-independent polynomial basis functions with time-dependent coefficients

$$Q_p^{(m)}(x, y, z, t) = \hat{Q}_{pl}^{(m)}(t)\, \Psi_l(x, y, z). \tag{2.22}$$

Here $\hat{Q}_{pl}^{(m)}$ introduces the time-dependent degrees of freedom and $\Psi_l(x,y,z)$ denotes the lth basis function transformed to the mth element. We can now employ an an affine linear coordinate transformation M from (x,y,z) to the reference element (ξ,η,ζ), obtaining

$$Q_p^{(m)}(x,y,z,t) = \hat{Q}_{pl}^{(m)}(t)\,\Psi_l(M(x,y,z)). \tag{2.23}$$

We can now define polynomial ansatz functions Φ_l on the reference element to discretize, thus getting

$$Q_p^{(m)}(x,y,z,t) = \hat{Q}_{pl}^{(m)}(t)\,\Phi_l^m(M(x,y,z)) \tag{2.24}$$

where M is the affine linear coordinate transformation from (x,y,z) to (ξ,η,ζ). The coordinate transformation increases the computational efficiency of the implementation as integrals in the reference system can be computed in advance. Thus Q_h is expressed in terms of the coordinate transformation as

$$\left[Q_H^{(m)}\right]_p(\xi,\eta,\zeta,t) = \hat{Q}_{pl}^m(t)\,\Phi_l(\xi,\eta,\zeta). \tag{2.25}$$

Following the DG-approach, we multiply 2.15 with the test function Φ_k and integrate over a tetrahedral element T^m, resulting in

$$\int_{\mathcal{T}^{(m)}} \Phi_k \frac{\partial Q_p}{\partial t} dV + \int_{\mathcal{T}^{(m)}} \Phi_k \left(A_{pq}\frac{\partial Q_q}{\partial x} + B_{pq}\frac{\partial Q_q}{\partial y} + C_{pq}\frac{\partial Q_q}{\partial z}\right) dV = 0. \tag{2.26}$$

To account for the discontinuities in Q_h fluxes F_p^h are added at the tetrahedron boundaries. After applying integration by parts the following equation is obtained

$$\int_{\mathcal{T}^{(m)}} \Phi_k \frac{\partial Q_p}{\partial t} dV + \int_{\partial\mathcal{T}^{(m)}} F_p^h dS - \int_{\mathcal{T}^{(m)}} \left(\frac{\partial \Phi_k}{\partial x} A_{pq}Q_q + \frac{\partial \Phi_k}{\partial y} B_{pq}Q_q + \frac{\partial \Phi_k}{\partial z} C_{pq}Q_q \right) dV = 0. \tag{2.27}$$

The calculation for the flux for the tetrahedrom $T^{(m)}$ and one of its neighboring tetrahedra T_j with $j = 1,2,3,4$ is as follows

$$\begin{aligned} F_p^h = &\frac{1}{2} T_{pq} \left(\tilde{A}_{qr}^{(m)} + \left|\tilde{A}_{qr}^{(m)}\right| \right) (T_{rs})^{-1} \hat{Q}_{sl}^{(m)} \Phi_l^{(m)} \\ &+ \frac{1}{2} T_{pq} \left(\tilde{A}_{qr}^{(m)} - \left|\tilde{A}_{qr}^{(m)}\right| \right) (T_{rs})^{-1} \hat{Q}_{sl}^{(m_j)} \Phi_l^{(m_j)}. \end{aligned} \tag{2.28}$$

There $\hat{Q}_{sl}^{(m)}\Phi_l^{(m)}$ and $\hat{Q}_{sl}^{(m_j)}\Phi_l^{(m_j)}$ represent the boundary extrapoladed values of the numerical solution from T^m and it's j-th side neighbour T^{m_j}, with

$$\left|\tilde{A}_{qr}^{(m)}\right| = R_{qp}^A \left|\Lambda_{ps}\right| (R_{sr})^{-1}. \tag{2.29}$$

Here $|\Lambda|$ is a diagonal matrix that contains the absolute value of the eigenvalues of the Jabobinan matrix $\tilde{A}_{qr}$, which must be aligned with the normal direction of the interface. The matrix R_{qp} holds the right eigenvectors of $\tilde{A}_{qr}$ as its colums. For a detailed calculation scheme the reader can refer to [Pue+07] Appendix A1.

To insert the numerical solution Q_h in 2.25 as well as the flux calculation 2.28, the subsequent equation as well as the spacial linear combination of the Jacobians

$$\begin{aligned} A^*_{pq} &= A_{pq}\frac{\partial \xi}{\partial x} + B_{pq}\frac{\partial \xi}{\partial y} + C_{pq}\frac{\partial \xi}{\partial z}, \\ B^*_{pq} &= A_{pq}\frac{\partial \eta}{\partial x} + B_{pq}\frac{\partial \eta}{\partial y} + C_{pq}\frac{\partial \eta}{\partial z}, \\ C^*_{pq} &= A_{pq}\frac{\partial \zeta}{\partial x} + B_{pq}\frac{\partial \zeta}{\partial y} + C_{pq}\frac{\partial \zeta}{\partial z}. \end{aligned} \tag{2.30}$$

must be transformed as the basis functions are defined on (ξ, η, ζ) using the following transformation

$$\mathrm{d}x\mathrm{d}y\mathrm{d}z = |J|\mathrm{d}\xi\mathrm{d}\eta\mathrm{d}\zeta, \tag{2.31}$$

with $|J|$ being the determinant of the Jacobian matrix J of the transformation. This results in the semi-discrete DG formulation of the ODE system inside the reference tetrahedron $\mathcal{T}_E$

$$\begin{aligned} &\frac{\partial \hat{Q}^{(m)}_{pl}}{\partial t}\,|J| \int_{\mathcal{T}_E} \Phi_k \Phi_l \, d\xi \, d\eta \, d\zeta \\ &+ \sum_{j=1}^{4} T^j_{pq} \frac{1}{2} \left(\tilde{A}^{(m)}_{qr} + \left| \tilde{A}^{(m)}_{qr} \right| \right) \left(T^j_{rs} \right)^{-1} \hat{Q}^{(m)}_{sl} \, |S_j| \, F^{-,j}_{kl} \\ &+ \sum_{j=1}^{4} T^j_{pq} \frac{1}{2} \left(\tilde{A}^{(m)}_{qr} - \left| \tilde{A}^{(m)}_{qr} \right| \right) \left(T^j_{rs} \right)^{-1} \hat{Q}^{(m_j)}_{sl} \, |S_j| \, F^{+,j,i,h}_{kl} \\ &- A^*_{pq} \hat{Q}^{(m)}_{ql} \, |J| \int_{\mathcal{T}_E} \frac{\partial \Phi_k}{\partial \xi} \Phi_l \, d\xi \, d\eta \, d\zeta \\ &- B^*_{pq} \hat{Q}^{(m)}_{ql} \, |J| \int_{\mathcal{T}_E} \frac{\partial \Phi_k}{\partial \eta} \Phi_l \, d\xi \, d\eta \, d\zeta \\ &- C^*_{pq} \hat{Q}^{(m)}_{ql} \, |J| \int_{\mathcal{T}_E} \frac{\partial \Phi_k}{\partial \zeta} \Phi_l \, d\xi \, d\eta \, d\zeta = 0, \end{aligned} \tag{2.32}$$

where $|S_j|$ is the area of the tetrahedron face j and

$$\begin{aligned} F^{-,j}_{kl} &= \int_{\partial(\mathcal{T}_E)_j} \Phi_k \left(\xi^{(j)}(\chi,\tau) \right) \Phi_l \left(\xi^{(j)}(\chi,\tau) \right) d\chi d\tau, \quad \forall 1 \le j \le 4, \\ F^{+,j,i,h}_{kl} &= \int_{\partial(\mathcal{T}_E)_j} \Phi_k \left(\xi^{(j)}(\chi,\tau) \right) \Phi_l \left(\xi^{(i)} \left(\tilde{\chi}^{(h)}(\chi,\tau), \tilde{\tau}^{(h)}(\chi,\tau) \right) \right) d\chi d\tau, \quad \forall 1 \le i \le 4, \quad 1 \le h \le 3. \end{aligned} \tag{2.33}$$

The flux matrix $F^{-,j}_{kl}$ refers to the flux contribution from the element m across its face j, whereas $F^{+,j,i,h}_{kl}$ corresponds to the contribution from the neighboring element k_j through the same face. The index i represents the local numbring of shared faces as viewed from the neighboring element. Similarly h specifies which of the neighboring element's local nodes correspoinds to the vertex at position 1 of the face j on m [DK06b].

2.2.2 ADER Time Discretization

Due to Bucher's barriers [But87], the efficiency of Runge-Kutta time-discretization schemes sinks radically as soon as the order of accuracy supersedes 4. To avoid this, the ADER approach is used on the semi-discrete formulation 2.32, thus achieving the same order of accuracy in both space- and time-discretization.

Time-derivatives are replaced using the Cauchy-Kovalewski procedure, which results in the kth time-derivative given by pure space derivatives in the reference system as

$$\frac{\partial^k Q_p}{\partial t^k} = (-1)^k \left(A^*_{pq} \frac{\partial}{\partial \xi} + B^*_{pq} \frac{\partial}{\partial \eta} + C^*_{pq} \frac{\partial}{\partial \zeta} \right)^k Q_q. \tag{2.34}$$

This equation is then used to substitute the time derivatives in a Taylor expanded Q_p with space derivatives. Combining the DG-approximation of 2.25 this results in

$$Q_p(\xi, \eta, \zeta, t) = \sum_{k=0}^{N} \frac{t^k}{k!} (-1)^k \left(A^*_{pq} \frac{\partial}{\partial \xi} + B^*_{pq} \frac{\partial}{\partial \eta} + C^*_{pq} \frac{\partial}{\partial \zeta} \right)^k \Phi_l(\xi, \eta, \zeta) \hat{Q}_{ql}(0). \tag{2.35}$$

The approximation is now projected onto each basis function and integrated analytically in time, which finally leads to the fully discrete ADER-DG scheme

$$\begin{aligned}
&\left[\left(\hat{Q}^{(m)}_{pl} \right)^{n+1} - \left(\hat{Q}^{(m)}_{pl} \right)^{n} \right] |J| M_{kl} + \\
&\frac{1}{2} \sum_{j=1}^{4} \left(T^j_{pq} \tilde{A}^{(m)}_{qr} (T^j_{rs})^{-1} + \Theta^j_{ps} \right) |S_j| F^{-,j}_{kl} \cdot I_{qlmn}(\Delta t) \left(\hat{Q}^{(m)}_{mn} \right)^n + \\
&\frac{1}{2} \sum_{j=1}^{4} \left(T^j_{pq} \tilde{A}^{(m)}_{qr} (T^j_{rs})^{-1} - \Theta^j_{ps} \right) |S_j| F^{+,j,i,h}_{kl} \cdot I_{qlmn}(\Delta t) \left(\hat{Q}^{(m)}_{mn} \right)^n - \\
&A^*_{pq} |J| K^{\xi}_{kl} \cdot I_{qlmn}(\Delta t) \left(\hat{Q}^{(m)}_{mn} \right)^n - B^*_{pq} |J| K^{\eta}_{kl} \cdot I_{qlmn}(\Delta t) \left(\hat{Q}^{(m)}_{mn} \right)^n - \\
&C^*_{pq} |J| K^{\zeta}_{kl} \cdot I_{qlmn}(\Delta t) \left(\hat{Q}^{(m)}_{mn} \right)^n = 0.
\end{aligned} \tag{2.36}$$

Here M_{kl}, F_{kl} and K_{kl} represent mass, flux and stiffness matrices, and $I_{plgm}(\Delta t)$ denotes the high-order ADER time integration operator applied to the degrees of freedom $(\tilde{Q}^{(m)}_{mn})^m$ at time level n.

The resulting formula makes updating variables from time level n to $n+1$ possible without storing intermediate states. Additionally an element $T^{(m)}$ only depends on its associated variables as well as its four direct neighbours $T^{(m_j)}$, $j = 1, ..., 4$. This makes it fitting for parallelization and more efficient that RK-DG schemes [DM05].

2.2.3 Boundary Conditions

Boundary conditions are crucial for ensuring that the physical behavior of waves at the domain's edges is correctly captured. Two primary types of boundary conditions are generally applied: absorbing boundaries and free-surface boundaries.

Absorbing boundaries

Absorbing boundary conditions are employed to prevent reflections from the boundaries of the computational domain. Waves exiting the domain should pass through the boundary without bouncing back, simulating an open boundary. This is achieved by setting the flux at the boundary to only consider outgoing waves. This is expressed as

$$F_p^{AbsorbBC} = \frac{1}{2} T_{pq} \left(\tilde{A}_{qr}^{(m)} + \left| \tilde{A}_{qr}^{(m)} \right| \right) \left(T_{rs} \right)^{-1} \hat{Q}_{sl}^{(m)} \Phi_l^{(m)}. \tag{2.37}$$

Free-Surface Boundaries

A free-surface boundary is where the elastic medium interfaces with a region free from external forces, such as air or a vacuum, therefore the normal and shear stresses must vanish. This is achieved using ghost cells where stresses are mirrored with the same magnitued but opposed signs. The resulting flux is

$$\begin{aligned} F_p^{FreeBC} = & \frac{1}{2} T_{pq} \left(\tilde{A}_{qr}^{(m)} + \left| \tilde{A}_{qr}^{(m)} \right| \right) \left(T_{rs} \right)^{-1} \hat{Q}_{sl}^{(m)} \Phi_l^{(m)} \\ & + \frac{1}{2} T_{pq} \left(\tilde{A}_{qr}^{(m)} - \left| \tilde{A}_{qr}^{(m)} \right| \right) \Gamma_{rs} \left(T_{st} \right)^{-1} \hat{Q}_{tl}^{(m)} \Phi_l^{(m)}, \end{aligned} \tag{2.38}$$

where the matrix $\Gamma_{rs} = diag\left(-1, 1, 1, -1, 1, -1, 1, 1, 1\right)$ is responsible for the aforementioned mirroring.

2.3 Summary

In this chapter, we have presented an overview of the governing equations for wave propagation in elastic media treated as a system of hyperbolic partial differential equations and numerical methods for solving said equations have been examined. Additionally boundary conditions that will be used have been introduced.

3 ITM

This chapter explores the concept of time-reversal methods, which are designed to reverse the propagation of waves, focusing them back to their source. Two main approaches exist to achieve this.

The first, known as the Time Reversal Mirror (TRM), relies on Cauchy boundary conditions. The wavefield in an entire volume V surrounded by surface S can be computed if said wavefield as well as its normal derivative are known in the entire S at all times t. Then the time reversal is achieved by recording the ougoing wave and radiating a time-reversed version from S.

The second approach involves altering the initial conditions withing the volume. This method mimics the hypothetical concept of Loschmidt's demon, where state of a system is reversed by instantaneously reversing the momentum of each particle inside said system, thus creating a time-reversed wave. In this approach the wavefield and its normal derivative are only known for a specific time and is called the Instantaneous Time Mirror (ITM).

This thesis solely deals with the ITM approach, where time-reversed seismic waves are created by a sudden wave propagation property modification in the medium. In this chapter the theoretical framework behind ITM will concisely be introduced avoiding excessive detail, particularly in the context on anisotropic elastic material.

3.1 Theory of Instantaneous Time Mirrors

Time-reversal methods for waves are based on the time-reversal invariance of wave equations. It exploits the principle that a wavefield can be fully reconstructed within a volume if both the field and its normal derivative are known on an enclosing surface. In anisotropic media the wave propagation becomes more complex due to the direction-dependent material properties governed by the stiffness tensor C_{ijkl}. The elastic wave equation for anisotropic media in its second-order vector form is written as [AR02]

$$\rho \ddot{\mathbf{U}}(\mathbf{x}, t) = C_{ijkl} \frac{\partial^2 U_k}{\partial x_j \partial x_l} + \mathbf{S}(\mathbf{x}, t), \tag{3.1}$$

where $\mathbb{U}(\mathbf{x}, t)$ is the displacement field and $\mathbb{S}(, t)$ is the source function. If said $\mathbb{S}$ is symmetric in time, meaning that $\mathbb{S}(, t) = \mathbb{S}(, -t)$, and $\hat{\mathbf{U}}(\mathbf{x}, t)$ is a solution, then $\hat{\mathbf{U}}(\mathbf{x}, -t)$ is an equally valid solution.

In anisotropic media, the stiffness of the material is directionally dependent, meaning that waves will propagate at different speeds depending on the direction and are determined

using the Christoffel matrix equation. The Christoffel matrix Γ is demined as

$$\Gamma_{ik}(\mathbf{n}) = C_{ijkl} n_j n_l \tag{3.2}$$

where n is the unit vector in the direction of wave propagaion. The Christoffel equation then represents an eigenvalue problem

$$\Gamma_{ik}(\mathbf{n}) U_k = \rho v^2 U_i \tag{3.3}$$

whose eigenvalues correspond to the wave velocities for the quasi P- wave and the two quasi S-wave polarizations. Now the wave impedance in anisotropic media can be derived. The formula valid in isotropy still holds $Z = \rho v$ [LeV02], but considering the direction dependent velocities now used in anisotropy, the impedance is also direction dependent

$$Z(\mathbf{n}) = \rho v(\mathbf{n}). \tag{3.4}$$

The ITM closely relates to Cauchy Initial Conditions. According to the Cauchy theorem, the evolution of a wave field can be completely determined from its values and derivatives at a single point in time. To create the time-reversed wave without the use of antennas or the full memory of the wave field [FF17], a sudden change in wave propagation properties, ie. impedance is introduced, which leads the initial conditions at two different points in time being modified.

3.2 Energy in the System Before and After ITM

The total energy E in a wave system constists of kinetic energy (related to particle velocity) and potential energy (related to the deformation of the material). The total energy of a propagation wave can be expressed as

$$E = \int \left(\frac{1}{2} \rho v^2 + \frac{1}{2} C \sigma^2 \right) dx, \tag{3.5}$$

where v is the particle velocity, σ is the stress and C is the elastic modulus. When an impedance change is introduced in ITM, these parameters are altered and cause a change in total energy. If we assume that the wave impedance has been scaled by introducing $\hat{\rho}$, which automatically results in a new velocity $vhat$, the updated energy of the system is described by the following equation

$$E = \int \left(\frac{1}{2} n^2 \rho (nv)^2 + \frac{1}{2} C \sigma^2 \right) dx. \tag{3.6}$$

When comparing the initial energy of the system with 3.6, it becomes clear that ITM leads to an energy change in the system. This can be visualized though calculating E_2/E_1, which results in

$$\frac{E_2}{E_1} = \frac{C\sigma^2 + n^3 \rho u^2}{C\sigma^2 + \rho u^2} \tag{3.7}$$

and gives 3.1 The miminum is clearly at $n = 1$, but since this suggests no velocity scaling and no reflections, so that it holds no relevance considering our objective.

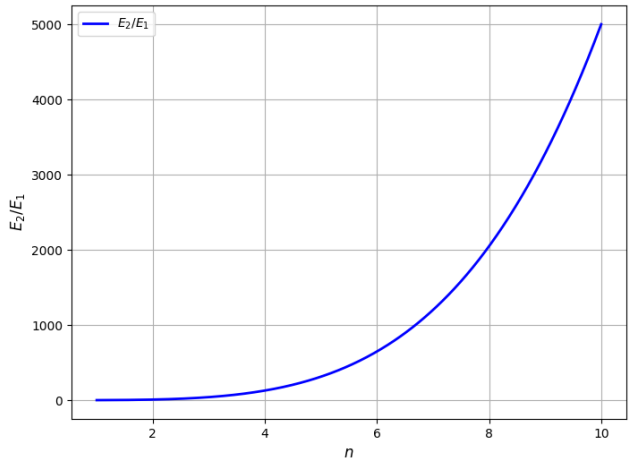

Figure 3.1: Energy of System $\left(\frac{E_2}{E_1}\right)$ during $t_{ITM}^{-} \leq t \leq t_{ITM}^{+}$, plotted for $n \in [1, 10]$

3.3 Summary

This chapter has given a short introduction on the different methods for achieving wave reflexions and explained the fundamental concepts behind the Instantaneous Time Mirror method. Aditionally the energy changes due to the ITM where analyzed.

4 Implementation

This chapter outlines the extensions made to SeisSol. The implementation is intentionally kept general as to ensure easy usability for future experiments. As outlined in previous chapters, to achieve the impedance change necessary for creating reflection waves, the material properties of the waves, specificaly their density ρ, is modified inside the time reversal period t^{-}_{ITM} to t^{+}_{ITM}. This impedance adjustment is essential to guarantee the formation of the reflected wave, as described in [LeV02]. In the following sections, we will explore different methods for achieving this impedance change to facilitate the desired wave reflection.

4.1 Wave Reflection in Anisotropic Media

The following section introduces various ways to modify the material parameters to achieve the necessary impedance impedance and reflect the waves.

4.1.1 Reflecting all waves by changing their velocities

This method involves adjusting the wave velocities by modifying the density ρ of the material while keeping the stiffness matrix components c_{ij} constant

$$\begin{aligned} \hat{c_{ij}} &= c_{ij}, \\ \hat{\rho} &= n^2 \rho. \end{aligned} \tag{4.1}$$

This results in a change of wave speeds and their respective impedances during the ITM as

$$\begin{aligned} \hat{v} &= nv, \\ \hat{Z} &= nZ \end{aligned} \tag{4.2}$$

where $\hat{v}$ and $\hat{Z}$ represent the velocities and impedances of the waves during the ITM process, and v and Z are their corresponding values before ITM.

4.1.2 Reflecting all waves by keeping their velocities constant

In this case the wave velocities are kept constant while still obtaining a modified impedance by adjusting the density ρ while also modifying the stiffness tensor compontnts c_{ij}. The material properties are modified as follows:

$$\begin{aligned} \hat{c_{ij}} &= nc_{ij}, \\ \hat{\rho} &= n\rho. \end{aligned} \tag{4.3}$$

which results in in the following impedance change during the ITM

$$\begin{aligned} \hat{v} &= v, \\ \hat{Z} &= nZ. \end{aligned} \tag{4.4}$$

4.1.3 Attempt to reflect only the quasi P-wave

An approach was explored to selectively reflect only the quasi P-wave by scaling the diagonal stiffness components while leaving the remaining ones unchanged. The goal was to modify the impedance of the quasi P-Wave without affecting the propagation of the quasi S-waves. The modification was carried out as follows:

$$\begin{aligned} \hat{c}_{11} &= n^2 c_{11}, \\ \hat{c}_{22} &= n^2 c_{22}, \\ \hat{c}_{33} &= n^2 c_{33}, \\ \hat{c}_{44} &= n^2 c_{44}, \\ \hat{c}_{55} &= n^2 c_{55}, \\ \hat{c}_{66} &= n^2 c_{66}, \\ \hat{\rho} &= \rho. \end{aligned} \tag{4.5}$$

However, this attempt did not successfully isolate the reflection of the quasi P-wave, all waves continued to exhibit reflections. This will be further discussed and analyzed in 5.

4.2 Eigenvalue Calculation and Time-Stepping

In this section, the role of eigenvalue calculation in determining the appropriate time-stepping scheme for wave propagation in anisotropic media will be discussed. These two aspects are tightly connected, as the maximum eigenvalues of the system matrices dictate the maximum permissible time stepbased on the CFL condition, which ensures stability in explicit time integration schemes.

Eigenvalue Calculation in Anisotropic Media

As laid out in 2.15, wave propagaion in anisotrpic media is governed by the following hyperbolic system of equations:

$$\frac{\partial Q_p}{\partial t} + A_{pq}\frac{\partial Q_q}{\partial x} + B_{pq}\frac{\partial Q_q}{\partial y} + C_{pq}\frac{\partial Q_q}{\partial z} = 0 \tag{4.6}$$

where Q is the state vecor representing the wave field, and A, B, and C are the flux Jacobian matrices corresponding to the wave propagation in the x-, y-, and z- directions respectively. These matrices are derived from the material properties of the medium and are directionally dependent. The eigenvalues of these matrices correspond to the characteristic wave speeds in

the respective directions. The eigenvalues of the matrix A were computed to determine said characteristic wave speeds and the largest eigenvalue was taken, which corresponds to the fastest wave speed in said direction. This process was repeated for matrices B and C in the y- and z- directions. These values are important for setting the time step size in the simulation, as the fastest wave determines the stability limit though the CFL condition.

Time-Stepping based on Eigenvalues

SeisSol utilizes Local Time Stepping (LTS), which assigns different time steps to various parts of the computational mesh. This approach tailors the time step to the local conditions, meaning regions with smaller elements or faster wave propagation speeds are updated more frequently, while areas with slower wave speeds or larger elements can afford larger time steps. This strategy enhances efficiency by focusing computational resources where they are most needed.

The time step for explicit time integration schemes must satisfy the CFL condition, which ensures that the numerical solution remains stable. In SeisSol, the stability chriterion

$$\Delta t^m < \frac{1}{2N+1}\frac{l^m}{v^m} \tag{4.7}$$

must be satisfied by each element for the time step size Δt^m. l^m and v^m denote the in-sphere diameter and maximum wave speed of element τ^m, N is the order of the method [WGB20]. As the maximum eigenvalue varies across directions in anisotropic media, the CFL condition must account for the largest wave speed in the domain.

When changes in material parameters occur, suchs as in the ITM process, the time step within each cluster must be updated accordingly. If the time step for cluster i is denoted as δi, this value is adjusted during TIM according to the changes in propagation speeds caused by modifications in the material properties in the follwoing way for different cases:

Reflecting all waves by changing their velocities or reflecting just the quasi P-wave

In this scenario, the time step is reduced in proportion to the scaling factor applied to the wave veocities. Therefore, for each cluster i, the time step is adjusted as follows:

$$\delta t_i = \frac{\delta t_i}{n}, \tag{4.8}$$

where δt represents the time step for cluster i during the ITM process.

Reflecting all waves by keeping their velocities constant

This this situation, there is no need to reduce the time step by factor n, since the wave velocities remain unchanged and only the impedance is altered As a result, the time step for each cluster remains the same,

$$\delta t_i = \delta t_i. \tag{4.9}$$

4.3 Summary

This chapter has discussed the implementation of the ITM method for wave reflection in anisotropic media. Various approaches were explored. Additionally, eigenvalue calculations and their role in determining time-stepping were addressed, along with the use of LTS in SeisSol.

5 Results and Discussion

In this chapter we analize and discuss the obtained results where the ITM is employed upon seismic waves. At first, we take a look at the time reversal of all seismic waves produced by a point source in an elastic medium. Then, we discuss the results of reflecting the waves under the same conditions but with their velocities held constant. Additionally the attempted reflection of only the quasi P-wave is discussed. Finally, we apply the method to a real-world scenario: an earthquake at Mount Zugspitze in the Alps.

5.1 Time-reversal of waves by point source in elastic media

Material Properties

The SISMOWINE test suite [Moc+06] offers a test case for seismic wave propagation in anisotropic materials using a geometry of a homogeneous full space. The material has a density ρ of 2700kg/m^3 and the elastic coefficients c_{ij} are as following

$$c = \begin{pmatrix} 97.2 & 10.0 & 30.0 & 0 & 0 & 0 \\ 10.0 & 97.2 & 30.0 & 0 & 0 & 0 \\ 30.0 & 30.0 & 70.0 & 0 & 0 & 0 \\ 0 & 0 & 0 & 32.4 & 0 & 0 \\ 0 & 0 & 0 & 0 & 32.4 & 0 \\ 0 & 0 & 0 & 0 & 0 & 43.6 \end{pmatrix} \text{ GPa.} \tag{5.1}$$

Mesh

Our mesh defines a cubic domain with dimensions [-20.000, 26.000] in each direction (x, y, z) with a higher resoltion around the seismic source, while getting coarser when moving away from it as seen in 5.1 An open space is simulated by applying absorbing boundaries to the surfaces of the cube, thus preventing reflections at the boundries.

Source

The source is a double point source and placed roughly in the middle of the domain at $(0, 0, 0)$. Is has a onset time of $t = 0.0s$, meaning the seismic activity begins at the very start of the simulation and it has only one non-zero Moment M_{xy}. The function $M_{xy}(t) = M_0 \cdot \frac{t}{T^2} \cdot \exp\left(-\frac{t}{T}\right)$ describes the moment rate time history with $T = 0.1$s being the characteristic time and maximal moment $M_0 = 8.9663 * 10^{17}$Nm.

ITM

The simulation is run for $t \in [0;5]$ with a step size of 0.5 and the ITM is started at $t = 2.0$. We thus expect to see the waves refocused at $t = 4.0$. To visualize the output we slice at (0, 0, 0), the source of the seismic event, in z-normal direction and plot the u-velocity.

Results

There are clearly three propagating waves present, which represent the quasi P-wave and quasi shear waves that where expected due to the nature of the material being anisotropic elastic 5.2. As the ITM is applied at $t = 2.0$, we would expect any reflected waves to show up in the subsequent time steps. Looking at said time-step plots in 5.3, it is clear that the ITM creates reflections of all waves present, successfully refocusing back to their origin, reaching it at $t = 4.0$ as was anticipated. After refocusing, the waves begin propagating outward again 5.4, but this is of no further relevance here as ITM was already successfully achieved.

This shows it is possible to simultaneously reflect all waves produced in an anisotropic medium in changing the impedance of all waves through modifying the material density to obtain a signal that is reflected back to its origin.

5.2 Time-reversal of waves under constant velocity

We now attempt to replicate the previous results obtained in 5.1 while applying an ITM with the velocities of the waves kept constant in the reflection phase. The same mesh and source and slice as in 5.1 is used.

The results in this case are nearly identical to those observed in 5.1, although a slight increase in wave strength was witnessed. Since SeisSol currently only supports energy output for isotropic elastic media, this will have to be inspected once is SeisSol is extended. All

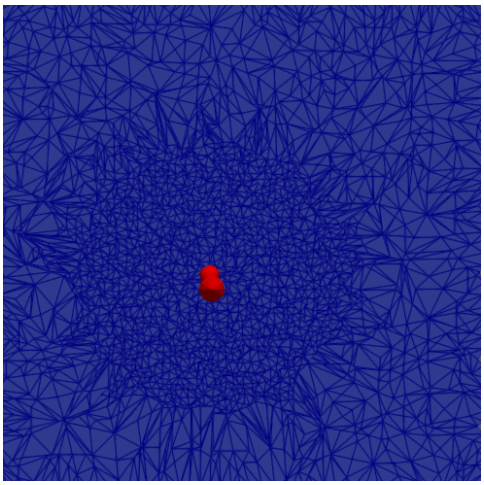

Figure 5.1: Mesh used in SISMOWINE simulations

three waves are reflected and refocused back to their origin at $t = 4.0$. Despite keeping the velocities constant during the reflexion phase, the wave behaviour follows the same pattern as in the previous case. This demonstrates that the ITM still successfully replicates the results when using the same initial conditions, regardless of whether the wave velocities are changed along with their impedances or not.

5.3 Time-reversal of P-wave

This section focuses on the time-reversal of exclusively the quasi P-wave in seismic wave propagation while allowing the other waves to continue propagating forward. Again the same mesh and source as in 5.1 is used and the visualization is done after applying the same slice. As evident in 5.5, the results revealed that full isolation of the quasi P-wave for reversal was unsuccessful. The complexities introduced by anisotropy alsongside the interaction between wave types in the media prevented decoupling the quasi P-wave from the quasi S-waves. Further refinement of the ITM approach is necessary to potentially achieve a precise P-wave reversal.

5.4 Test Case: Mount Zugspitze

5.4.1 Source positioned 10km under the surface

To further strengthen our concept, we now attempt to provide an application example of reflecting seismic waves around the Zugspitze in the Bavarian Alps, thus validating the potential of this implementation to solve real geophysics problems.

Material Properties

The material properties represent an anisotropic elastic medium roughly typical for the Earth's crust in the Alps region. The material density is set to 2670kg/m^3 and the stiffness coefficients are defined as

$$c_{ij} = \begin{pmatrix} 231.65 & 84.55 & 73.99 & -2.27 & -3.31 & -24.03 \\ 84.55 & 268.07 & 71.25 & -1.60 & -1.94 & -34.73 \\ 73.99 & 71.25 & 221.22 & -6.06 & -8.22 & 4.42 \\ -2.27 & -1.60 & -6.06 & 77.75 & -4.59 & -1.47 \\ -3.31 & -1.94 & -8.22 & -4.59 & 74.91 & -1.93 \\ -24.03 & -34.73 & 4.42 & -1.47 & -1.93 & 98.27 \end{pmatrix} \text{GPa}. \tag{5.2}$$

Mesh

The region around Mount Zugspitze is discretized into a tetrahedral computational mesh spanning 90 km × 90 km horizontally and extending to a depth of 70 km. It has a resolution of 600m at the surface and contains 1.47 million cells.

Source

A kinematic source point located at the center of the domain and placed at a depth of 10km. The source parameters are identical to the LOH1 test case also used in 5.1.

ITM

The seismic waves are simulated for $t \in [0;5]$. The mesh is sliced at its source point in z-direction and the u-velocity is plotted to visualize the propagation. The waves take on an elliptical shape, demonstrating the directional dependency of wave speed in anisotropic media 5.7. At $t = 2.5$ the ITM is initiated, which begins to reflect the waves back toward the origin. As the simulation progresses, each time step shows the waves being reflected and gradually collapsing back toward the source 5.8. By $t = 4.5$ additional waves begin to appear. These unexpected waves are not explained but could be attributed to artificial reflections caused by numerical instabilities or internal wave interactions. However, the intended wave reflections, triggered by ITM, remain unaffected by these additional waves and successfully collapse at their origin at $t = 5.0$ as expected.

Results

These results demonstrate that the ITM method can be successfully applied to reflect and refocus seismic waves in complex anisotropic media. Despite the appearance of additional, unexplained waves, the primary wave reflection remained unaffected.

5.4.2 Source positioned 500m under the surface

The same experiment as in 5.4.1 was conducted, reusing the material properties, mesh and simulation parameters, but using a slightly stronger source positioned only 500m beneath the surface to ensure that the wave propagation could be clearly visualized at the surface level. 5.9 Due to reflections the ITM is slightly unclear due to other reflections, yet still present. An example is included in 5.9.

This result strengthens the potential application of the ITM for scenarios where wave reflections occur close to the Earth's surface.

5.5 Summary

In this chapter, the results of applying the ITM to various seismic wave scenarios were analyzed. Initially the results of the time-reversal of waves generated by a point source in an elastic medium were presented. This was replicated while keeping the wave velocities constant during ITM. Then it was unsuccessfully attempted to isolate the quasi P-wave for reversal while allowing the quasi S-waves to propagate forward. Finally the ITM was applied to a real-world test case at Mount Zugspitze.

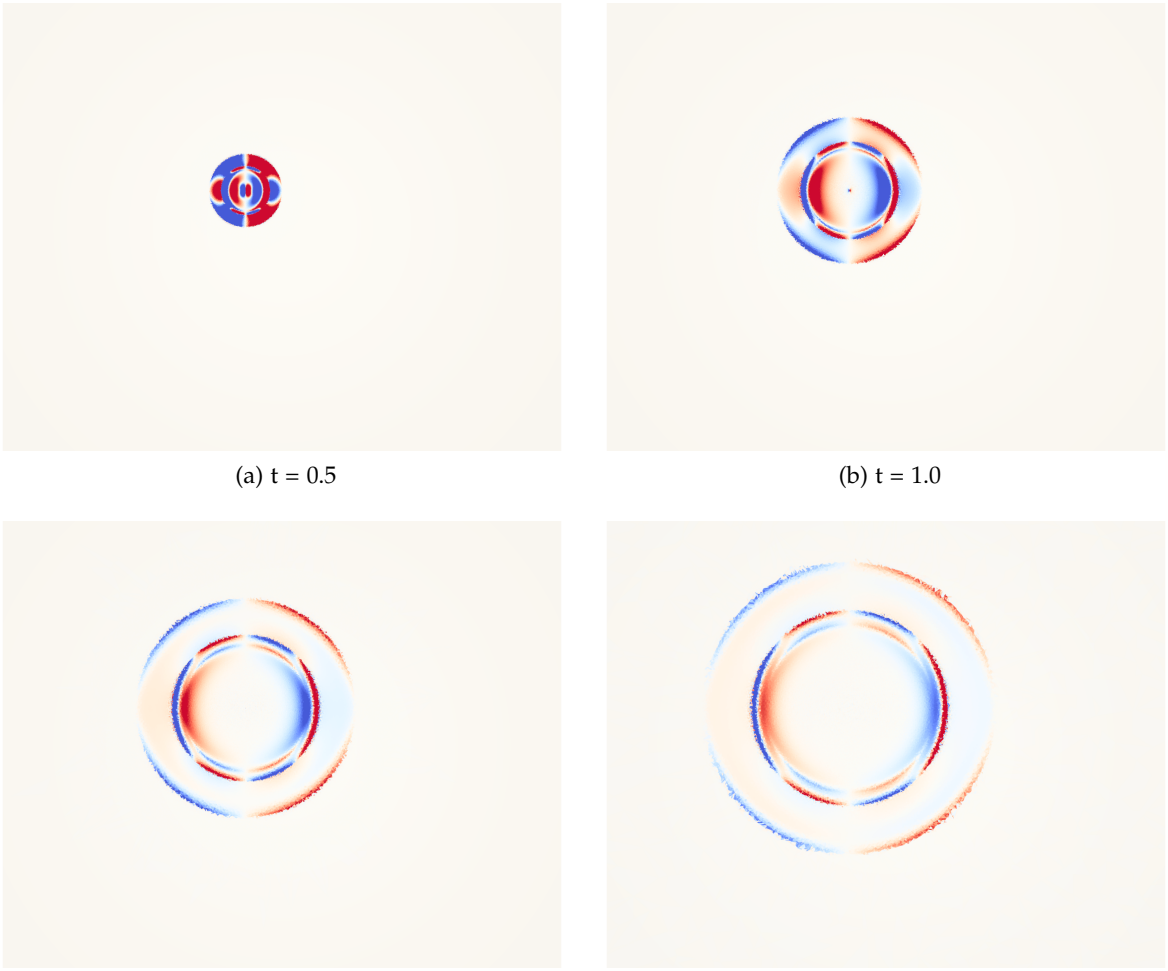

(a) t = 0.5

(b) t = 1.0

(c) t = 1.5

(d) t = 2.0

Figure 5.2: Wave propagation in anisotropic elastic medium after point source initiation at $t = 0.0$.

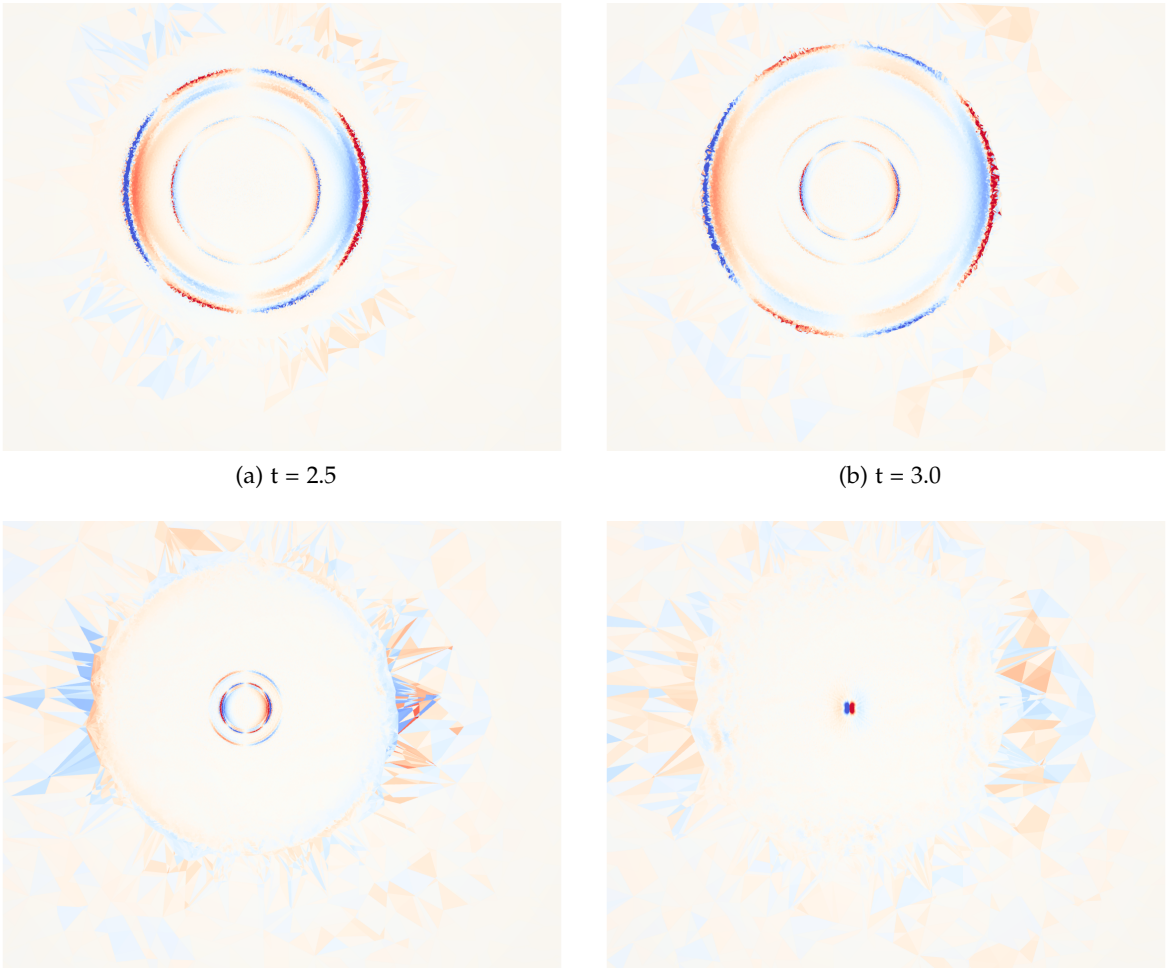

(a) t = 2.5

(b) t = 3.0

(c) t = 3.5

(d) t = 4.0

Figure 5.3: Waves reflecting back to origin after ITM was applied at $t = 2.0$ and collapsing back at the origin at $t = 4.0$.

(a) t = 4.0

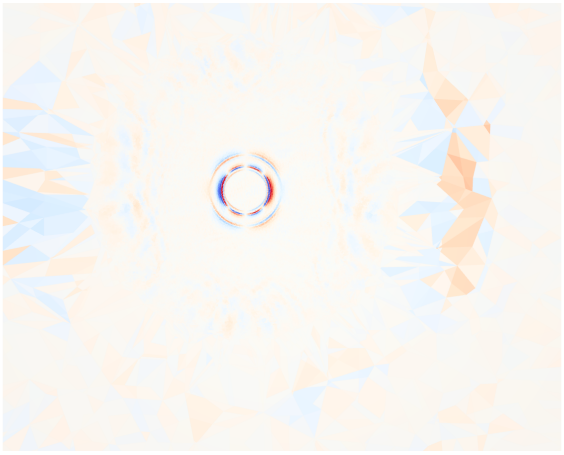

(b) t = 4.5

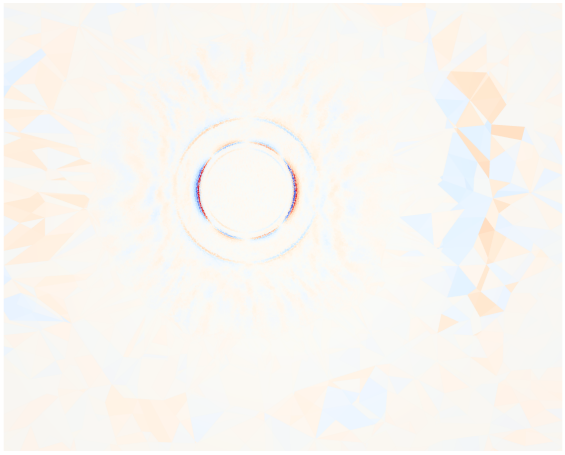

(c) t = 5.0

Figure 5.4: After recollapsing at the source point at $t = 4.0$, refocused waves diverge again.

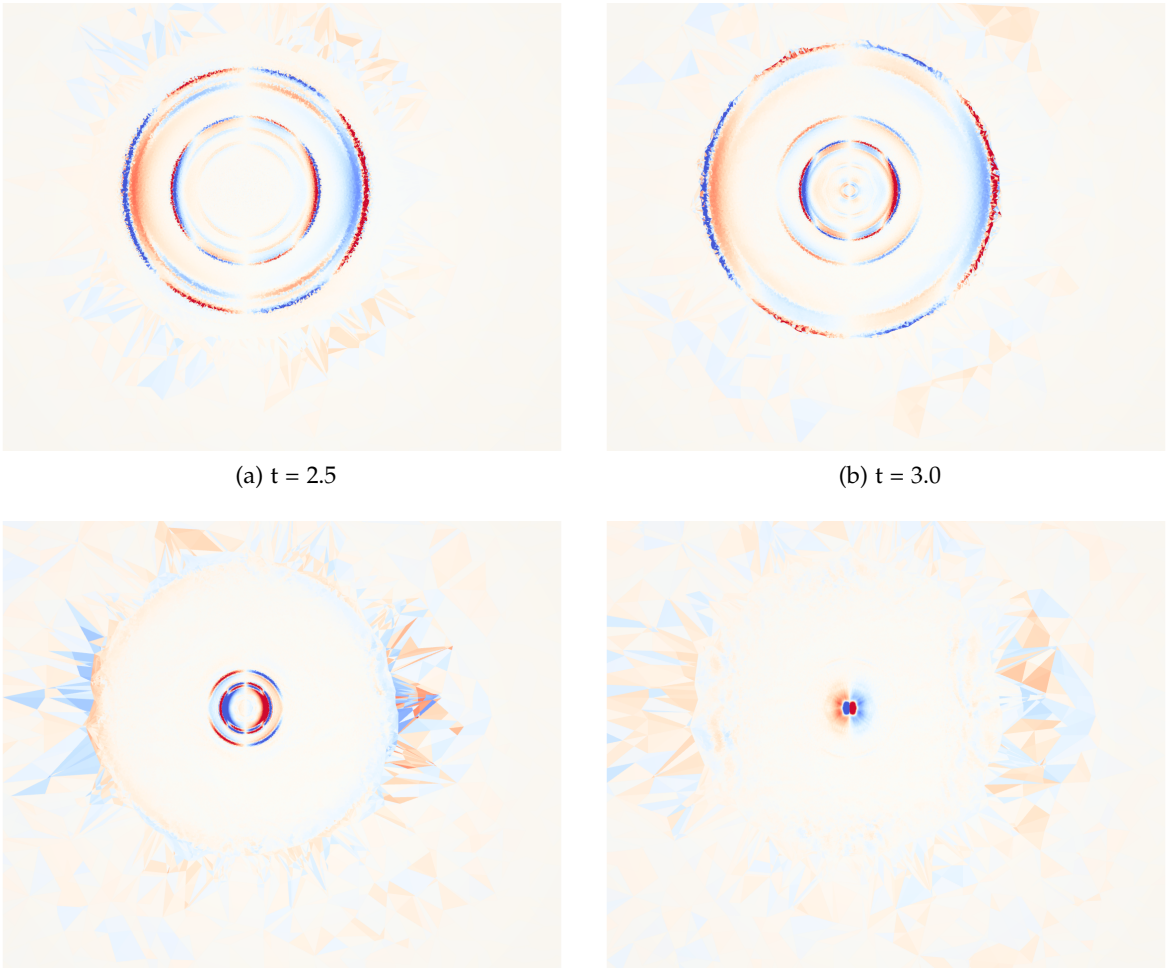

(a) t = 2.5

(b) t = 3.0

(c) t = 3.5

(d) t = 4.0

Figure 5.5: After ITM was applied at $t = 2.0$, while the waves still reflect back to the origin, clearly not only the quasi P-wave is being reflected as intended.

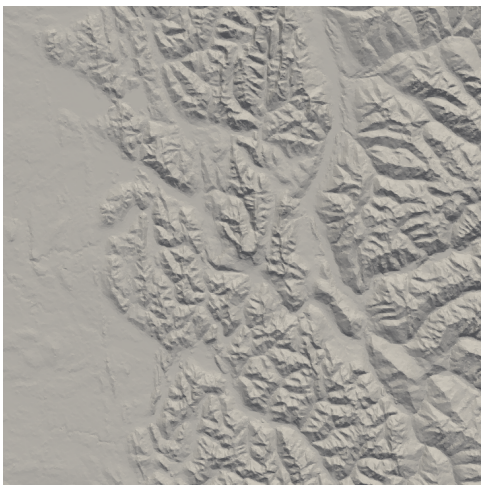

Figure 5.6: Used topology around Mount Zugspitze.

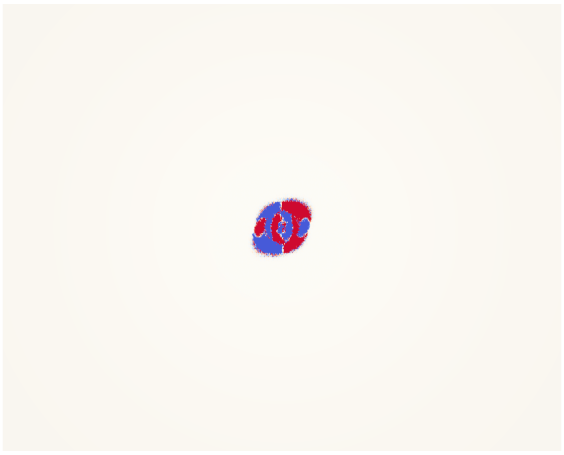

(a) t = 0.5

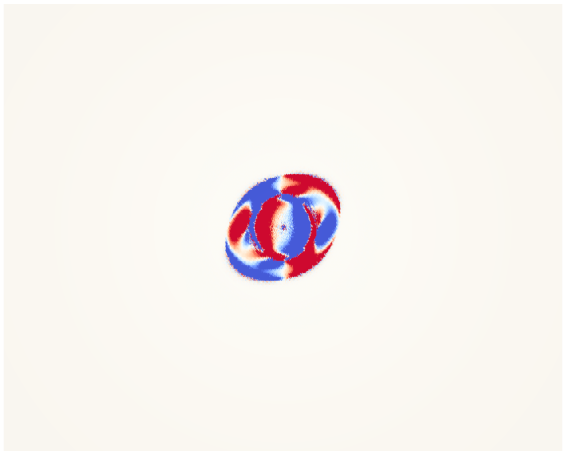

(b) t = 1.0

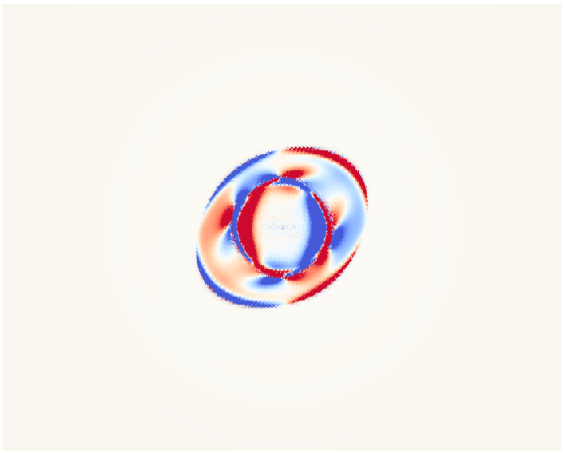

(c) t = 1.5

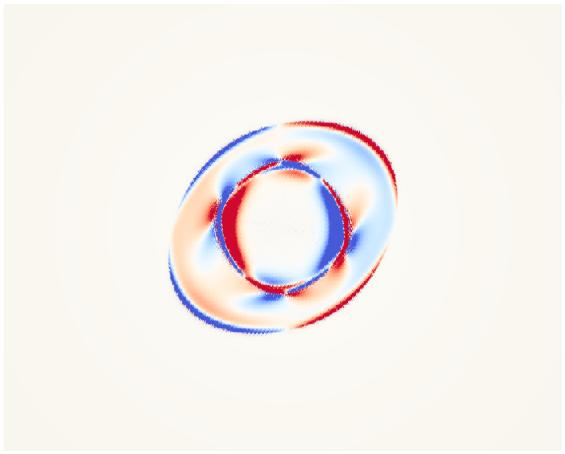

(d) t = 2.0

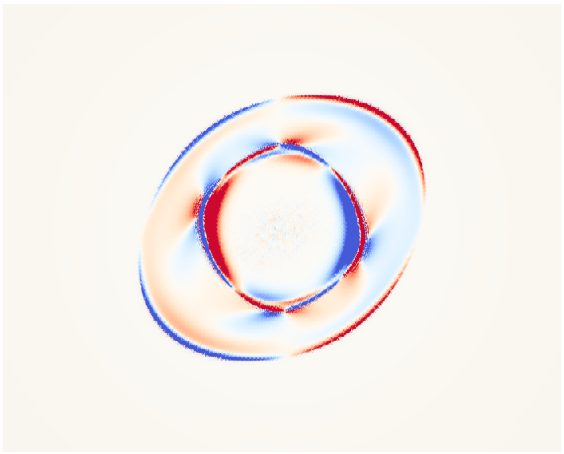

(e) t = 2.5

Figure 5.7: Wave propagation around Mount Zugspitze after point source initiation at $t = 0.0$, sliced 10km beneath the surface.

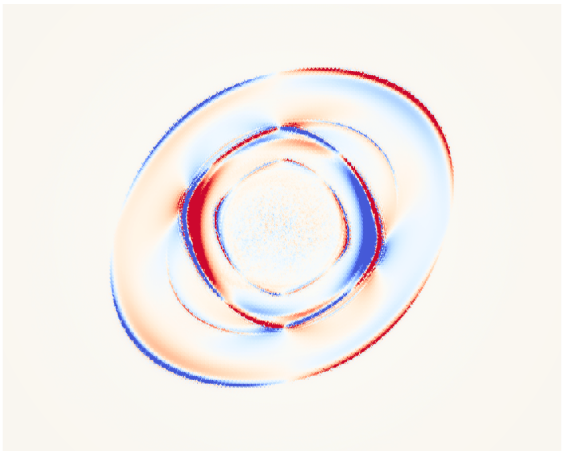

(a) t = 3.0

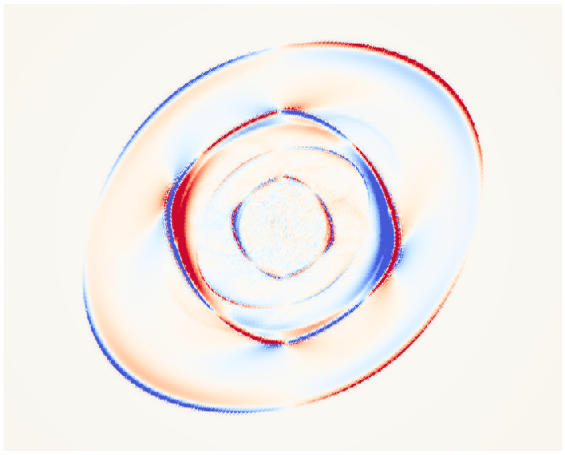

(b) t = 3.5

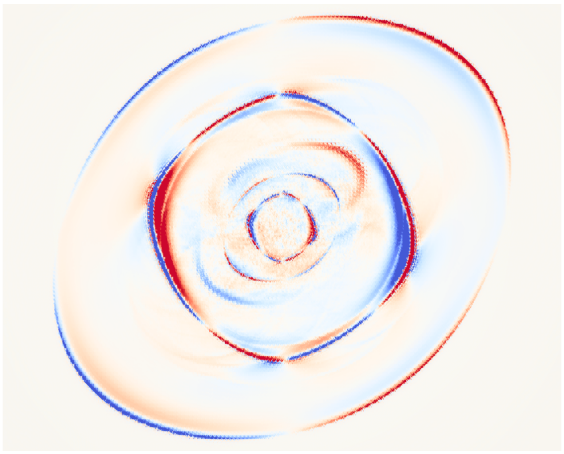

(c) t = 4.0

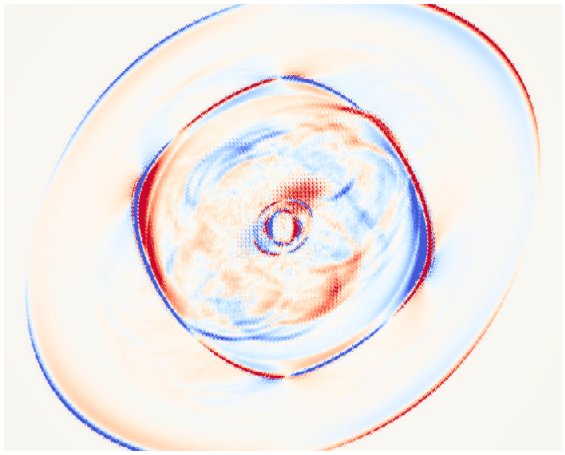

(d) t = 4.5

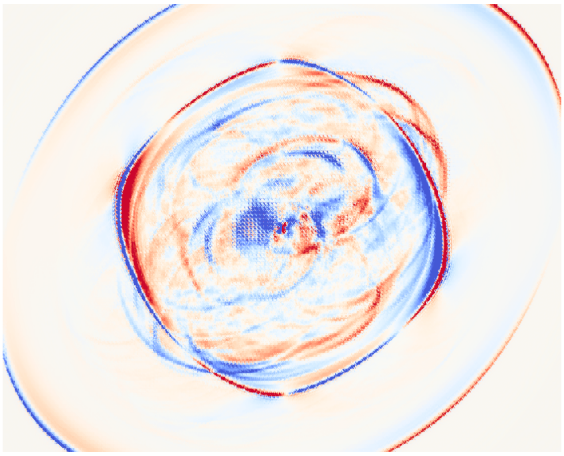

(e) t = 5.0

Figure 5.8: Mount Zugspitze, sliced at -10km: Waves reflecting back to origin after ITM was applied at $t = 2.5$ and collapsing back at the origin at $t = 5.0$.

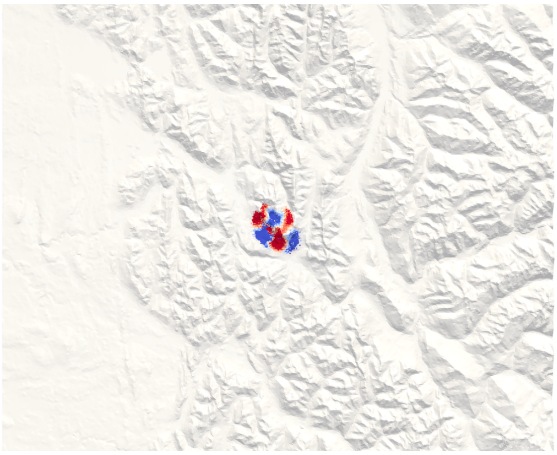

(a) t = 0.5

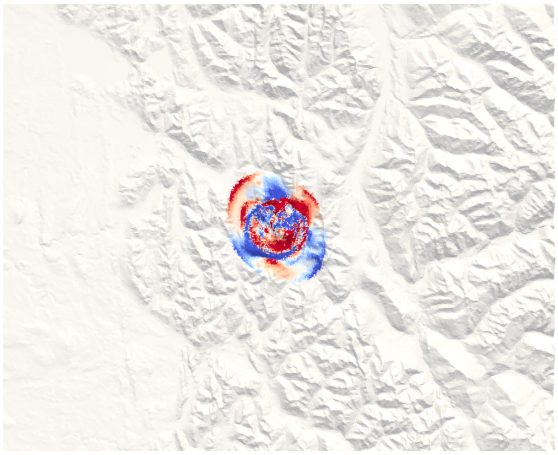

(b) t = 1.0

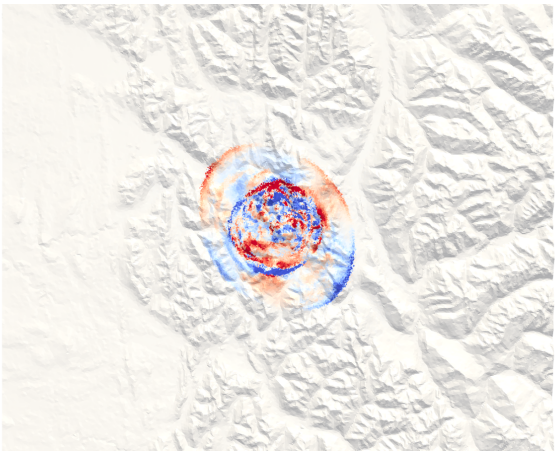

(c) t = 1.5

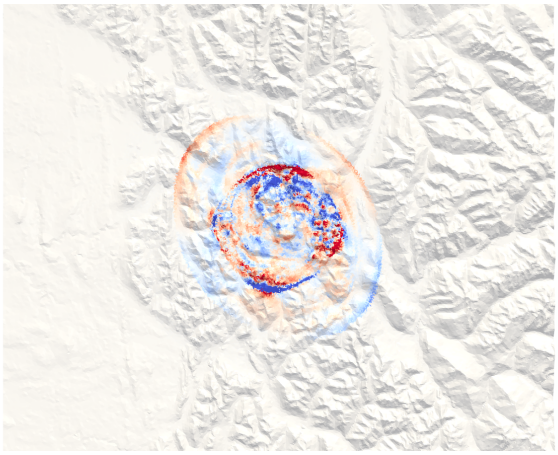

(d) t = 2.0

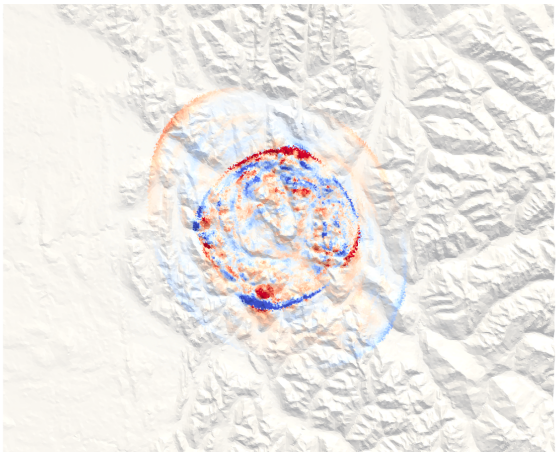

(e) t = 2.5

Figure 5.9: Wave propagation at the surface of Mount Zugspitze after point source initiation at $t = 0.0$.

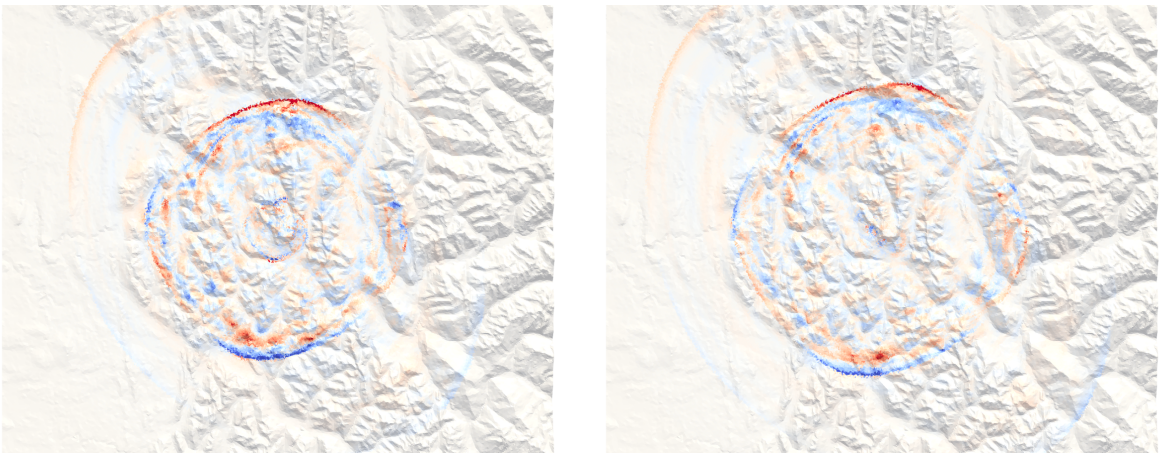

(a) t = 4.0 (b) t = 4.5

Figure 5.10: Surface of Mount Zugspitze: Waves reflecting back to origin after ITM was applied at $t = 2.5$ at time $t = 4.0$ and $t = 4.5$. The reflected waves will reach their origin at $t = 5.0$, 500m beneath the surface.

6 Conclusions and Outlook

In this thesis, we explored the application of the Instantaneous Time Mirror (ITM) to seismic wave propagation, specifically focusing on anisotropic media, and its implementation in the numerical simulation software SeisSol. Initially, the theoretical background of wave propagation was introduced in Chapter 2, covering the basic principles of anisotropic elastic wave theory. Additionally, the numerical scheme ADER-DG used in SeisSol was presented. Chapter 3 centered on the theory behind the ITM method, explaining how impedance discontinuity leads to wave reflections. It also covered the transition from isotropic to anisotropic elastic media and the challenges this introduced. Additionally, the energy behavior was analyzed for various ITM stages. Chapter 4 focused on the implementation details. The numerical method to simulate the ITM process was described. The implementation of various wave reversal scenarios where differentiated. In Section 4.2 the challenges of handling time-stepping were touched upon.

Chapter 5 presented the results of applying the ITM method to various seismic scenarios, showcasing its effectiveness in different settings. In Section 5.1, we explored the time-reversal of waves generated by a point source in an elastic medium. This demonstrated the ITM's ability to successfully reverse both quasi P-wave and quasi S-waves, retracing them back to the point source as expected. This result was successfully replicated using ITM with constant velocities. Section 5.3 focused on an attempt to reverse only the quasi P-wave while allowing the quasi S-waves to continue forward. This was not successful, indicating that additional adjustments in the method are needed to isolate the quasi P-wave. Finally, Section 5.4 presented a real-world test case based on Mount Zugspitze. This case provided a more complex and realistic environment to assess the ITM method. The result demonstrated that the ITM could handle realistic geological features and confirmed that wave reversal is feasible in more intricate environments.

While this thesis has successfully provided an implementation of ITM for anisotropic seismic waves, several areas still require further exploration. The ITM parameters are currently being chosen heuristically and an analytical solution could be determined. Additionally, while this thesis has demonstrated the method's effectiveness through experimental applications, an analytical analysis of the ITM could further enhance understanding. The ITM could also be studied in different scenarios like visco- and poroelastic media. Further work will be needed to inspect the possibility of achieving successful reflection of an isolated P- or S-wave.

Abbreviations

DG Discontinuous Galerkin
FE Finite Element
TRM Time Reversal Mirror
ITM Instantaneous Time Mirror
DG Discontinuous Galerkin
ADER Arbitrary high-order schemes using DERivates
DG-FE Discontinuous Galerkin Finite Element
RK-DG Runge Kutta Discontinuous Galerkin
CFL Courant-Friedrichs-Lewy
LTS Local Time Stepping
PDE Partial Differential Equation

List of Figures

Bibliography

[AR02] K. Aki and P. G. Richards. *Quantitative Seismology*. 2nd. University Science Books, 2002. ISBN: 0935702962.

[Bon76] W. L. (L. Bond. *Crystal technology*. eng. Wiley series in pure and applied optics. New York: Wiley, 1976. ISBN: 0471087653.

[But87] J. C. Butcher. *The Numerical Analysis of Ordinary Differential Equations: Runge-Kutta and General Linear Methods*. USA: Wiley-Interscience, 1987. ISBN: 0471910465.

[DK06a] M. Dumbser and M. Käser. "An arbitrary high-order discontinuous Galerkin method for elastic waves on unstructured meshes — II. The three-dimensional isotropic case". In: *Geophysical Journal International* 167.1 (Oct. 2006), pp. 319–336. ISSN: 0956-540X. DOI: 10.1111/j.1365-246X.2006.03120.x.

[DK06b] M. Dumbser and M. Käser. "An arbitrary high-order discontinuous Galerkin method for elastic waves on unstructured meshes — II. The three-dimensional isotropic case". In: *Geophysical Journal International* 167.1 (Oct. 2006), pp. 319–336. ISSN: 0956-540X. DOI: 10.1111/j.1365-246X.2006.03120.x. eprint: https://academic.oup.com/gji/article-pdf/167/1/319/6021938/167-1-319.pdf. URL: https://doi.org/10.1111/j.1365-246X.2006.03120.x.

[DM05] M. Dumbser and C.-D. Munz. "ADER Discontinuous Galerkin Schemes for Aeroacoustics". In: *Comptes Rendus Mécanique* 333 (2005), pp. 683–. DOI: 10.1016/j.crme.2005.07.008.

[FF17] M. Fink and E. Fort. "From the time-reversal mirror to the instantaneous time mirror". In: *The European Physical Journal Special Topics* 226.7 (May 2017), pp. 1477–1486. ISSN: 1951-6401. DOI: 10.1140/epjst/e2016-60258-8.

[Käs+10] M. Käser, C. Castro, V. Hermann, and C. Pelties. "SeisSol – A Software for Seismic Wave Propagation Simulations". In: *High Performance Computing in Science and Engineering, Garching/Munich 2009*. Ed. by S. Wagner, M. Steinmetz, A. Bode, and M. M. Müller. Berlin, Heidelberg: Springer Berlin Heidelberg, 2010, pp. 281–292. ISBN: 978-3-642-13872-0.

[LeV02] R. J. LeVeque. *Finite Volume Methods for Hyperbolic Problems*. Cambridge Texts in Applied Mathematics. Cambridge University Press, 2002. DOI: 10.1017/CBO9780511791253.

[Moc+06] P. Moczo, J. P. Ampuero, J. Kristek, S. DAY, M. KRISTEKOVA, P. Pazak, M. Galis, and H. Igel. "Comparison of Numerical Methods for Seismic Wave Propagation and Source Dynamics - the SPICE Code Validation". In: (Aug. 2006).

[OM03] D. A. Okaya and T. V. McEvilly. "Elastic wave propagation in anisotropic crustal material possessing arbitrary internal tilt". In: *Geophysical Journal International* 153.2 (May 2003), pp. 344–358. ISSN: 0956-540X. DOI: 10.1046/j.1365-246X.2003.01896.x. eprint: https://academic.oup.com/gji/article-pdf/153/2/344/1730914/153-2-344.pdf. URL: https://doi.org/10.1046/j.1365-246X.2003.01896.x.

[Pue+07] J. de la Puente, M. Käser, M. Dumbser, and H. Igel. "An arbitrary high-order discontinuous Galerkin method for elastic waves on unstructured meshes - IV. Anisotropy". In: *Geophysical Journal International* 169.3 (June 2007), pp. 1210–1228. ISSN: 0956-540X. DOI: 10.1111/j.1365-246X.2007.03381.x. eprint: https://academic.oup.com/gji/article-pdf/169/3/1210/6081673/169-3-1210.pdf. URL: https://doi.org/10.1111/j.1365-246X.2007.03381.x.

[TMN01] E. F. Toro, R. C. Millington, and L. A. M. Nejad. "Towards Very High Order Godunov Schemes". In: *Godunov Methods: Theory and Applications*. Ed. by E. F. Toro. New York, NY: Springer US, 2001, pp. 907–940. ISBN: 978-1-4615-0663-8. DOI: 10.1007/978-1-4615-0663-8_87.

[WGB20] S. Wolf, A.-A. Gabriel, and M. Bader. "Optimization and Local Time Stepping of an ADER-DG Scheme for Fully Anisotropic Wave Propagation in Complex Geometries". en. In: *Computational Science - ICCS 2020*. Ed. by V. Krzhizhanovskaya, G. Závodszky, M. Lees, J. Dongarra, P. Sloot, S. Brissos, and J. Teixeira. Lecture Notes in Computer Science 12139. Springer, June 2020, pp. 32–45. DOI: 10.1007/978-3-030-50420-5_3. URL: https://link.springer.com/chapter/10.1007/978-3-030-50420-5_3.